STRUCTURAL BIOLOGY

Structural insights into G protein activation by D1 dopamine receptor

Xiao Teng[1,2]†, Sijia Chen[2,3]†, Qing Wang[2,4], Zhao Chen[1,2], Xiaoying Wang[2], Niu Huang[1,2], Sanduo Zheng[1,2,3]*

G protein–coupled receptors (GPCRs) comprise the largest family of membrane receptors and are the most important drug targets. An agonist-bound GPCR engages heterotrimeric G proteins and triggers the exchange of guanosine diphosphate (GDP) with guanosine triphosphate (GTP) to promote G protein activation. A complete understanding of molecular mechanisms of G protein activation has been hindered by a lack of structural information of GPCR–G protein complex in nucleotide-bound states. Here, we report the cryo-EM structures of the D1 dopamine receptor and mini-G_s complex in the nucleotide-free and nucleotide-bound states. These structures reveal major conformational changes in Gα such as structural rearrangements of the carboxyl- and amino-terminal α helices that account for the release of GDP and the GTP-dependent dissociation of Gα from Gβγ subunits. As validated by biochemical and cellular signaling studies, our structures shed light into the molecular basis of the entire signaling events of GPCR-mediated G protein activation.

INTRODUCTION

More than 800 G protein–coupled receptors (GPCRs) in the human genome mediate numerous physiological functions by responding to a wide range of stimuli including light, odors, hormones, and neurotransmitters (*1*, *2*). Agonist binding to a GPCR induces its conformational changes, which subsequently lead to the engagement of guanosine diphosphate (GDP)–bound Gαβγ heterotrimer. Structural rearrangement of Gα when bound to GPCR results in the exchange of GDP for guanosine triphosphate (GTP) and the dissociation of heterotrimer (*3*). G proteins are divided into three major subfamilies: adenylyl cyclase stimulatory G protein ($G\alpha_s$), adenylyl cyclase inhibitory G protein ($G\alpha_{i/o}$), and $G\alpha_{q/11}$, on the basis of distinct downstream signaling pathways (*4*). Understanding molecular mechanisms of G protein activation and selectivity has been the subject of intensive research. The first crystal structure of the β2-adrenergic receptor (β2AR)–G_s complex in the nucleotide-free state revealed outward movement of transmembrane (TM5) and TM6 in β2AR when coupling to G protein compared with the inactive β2AR, which creates a large cytosolic pocket of β2AR (*5*). The C-terminal helix (α5) of $G\alpha_s$ displaced toward the receptor and inserted into the cytosolic pocket of the β2AR. The conformational changes of the GPCR–G protein interface allosterically induce structural rearrangement of the nucleotide-binding pocket, leading to the separation of the α-helical domain (AHD) of the Gα subunit from the Ras-like domain (Ras) and the subsequent release of GDP. In complement to structural studies, hydrogen/deuterium exchange–mass spectrometry (HDX-MS) (*6*, *7*), double electron-electron resonance (DEER) spectroscopy (*8*), and molecular dynamics (MD) studies (*9*) have shown that both the AHD and Ras domain separation and the conformational change of the nucleotide-binding pocket caused by GPCR–G protein interaction are necessary to promote the GDP release.

Since the report of the first crystal structure of the β2AR-G_s complex, an increasing number of structures of the GPCR–G protein complex were obtained by single-particle cryo–electron microscopy (cryo-EM) (*10*–*12*). These are attributable to the use of scaffold proteins (*5*, *13*, *14*) to stabilize the GPCR–G protein complex and modified thermostable G proteins (mini-G) (*15*), as well as the technical breakthroughs in cryo-EM (*16*). However, all of these complex structures solved so far are in the nucleotide-free state, which only provide a snapshot of a stable intermediate state. The GPCR–G protein coupling events are obviously highly dynamic and comprise a series of intermediate states. A recent crystal structure of β2AR in complex with a C-terminal peptide of $G\alpha_s$ revealed a different configuration from the β2AR–G protein complex, providing additional insights into the molecular basis of G protein selectivity (*17*). Clearly, it is important to obtain intermediate states of GPCR–G protein complex including GDP- and GTP-bound states at atomic level to fully understand the molecular mechanisms of G protein selectivity and G protein activation. However, instability of the GPCR–G protein complexes in the nucleotide-bound state makes them intractable to structural studies.

Dopamine exerts a variety of physiological functions through five distinct G protein–coupled dopamine receptor (DR) subtypes (D1R to D5R), including locomotor activity and reward (*18*–*20*). Dysfunction of the dopaminergic system has been linked to Parkinson's disease and psychiatric diseases. DRs are classified as two subfamilies: the D1-like (D1R and D5R) and the D2-like (D2R, D3R, and D4R). Although DRs share high sequence similarity in the transmembrane region involved in G protein binding, D1-like receptors couple to G_s, while D2-like receptors couple to $G_{i/o}$ (Fig. 1A). Recently published cryo-EM structures of D1R-G_s and D2R-$Gi_{/o}$ with various ligands provided structural insight into ligand recognition and G protein selectivity (*21*–*25*). In this study, to better understand the molecular basis of G protein selectivity and activation, we sought to determine the cryo-EM structures of the D1R-G_s complex in both nucleotide-free and nucleotide-bound states.

[1]Tsinghua Institute of Multidisciplinary Biomedical Research, Tsinghua University, Beijing, China. [2]National Institute of Biological Sciences, Beijing, China. [3]Graduate School of Peking Union Medical College, Beijing, China. [4]School of Pharmaceutical Science and Technology, Tianjin University, Tianjin, China.
*Corresponding author. Email: zhengsanduo@nibs.ac.cn
†These authors contributed equally to this work.

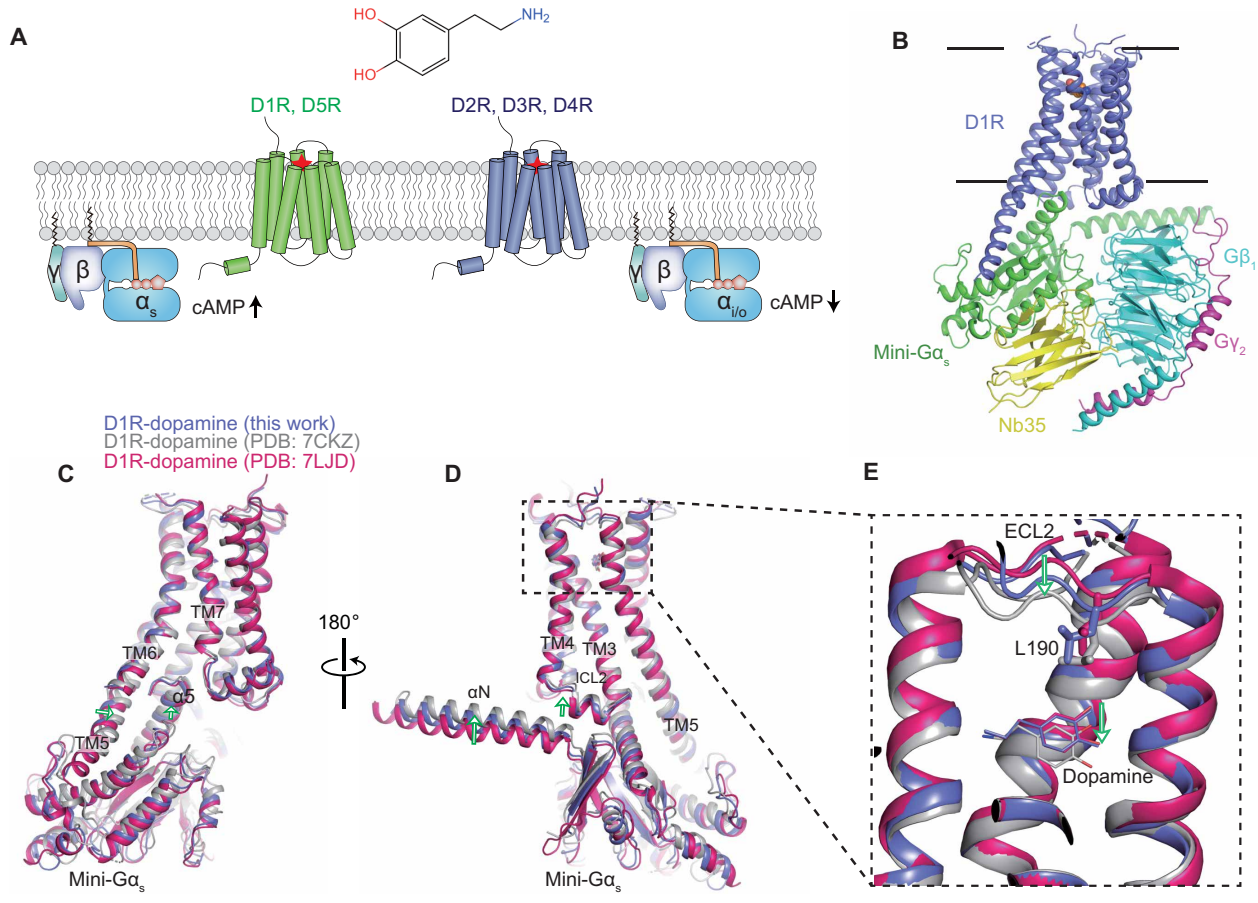

Fig. 1. Structure of the dopamine-bound D1R–G protein complex in the nucleotide-free state. (**A**) Distinct G protein selectivity of five DRs (D1R to D5R). (**B**) Overall architecture of dopamine-bound D1R–mini-G_s–Nb35 complex. D1R, mini-$G\alpha_s$, $G\beta_1$, $G\gamma_2$, and Nb35 are colored in blue, green, cyan, magenta, and yellow, respectively. (**C** and **D**) Structural superposition of the dopamine-bound D1R-G_s complex structure in this study and dopamine-bound structures of the same complex in previous studies in two opposite views. Receptors from three structures are aligned. $G\beta_1$, $G\gamma_2$, and Nb35 are omitted for clarity. Conformational changes are shown with green arrows. (**E**) Close-up views of the dopamine-binding pocket. L190 at ECL2 involved in hydrophobic interaction with dopamine is shown as stick. cAMP, cyclic adenosine 3′,5′-monophosphate.

RESULTS AND DISCUSSION

Structures of the dopamine-bound D1R–mini-G_s complex

To enhance the stability of the D1R-G_s complex and simplify the purification process, we created a fusion protein (D1R–mini-$G\alpha_s$) where the C terminus of the wild-type human D1R is fused to the N terminus of mini-$G\alpha_s$ (*15*), which is an engineered thermostable G_s without the AHD domain. We expressed D1R–mini-$G\alpha_s$ in Expi293 cell by transient transfection and purified it by antibody affinity chromatography. To assemble the D1R–mini-G protein complex, the purified D1R–mini-$G\alpha_s$ was mixed with the excess Nb35 (*5*) that has been used to stabilize the GPCR–G protein complex and human $G\beta_1\gamma_2$ subunits and further purified to homogeneity by size exclusion chromatography (fig. S1A). Structures of the dopamine-bound D1R–mini-G_s complex in the nucleotide-free state, GDP-bound state, and the GTP state were determined at nominal resolutions from 3.1 to 4.2 Å (figs. S1 to S5 and table S1). Small molecules including dopamine and GDP, except GTP, can be unambiguously modeled owing to the excellent quality of the EM density map. Because of the high stability of the D1R–mini-G_s fusion protein complex and no orientation preference, we were able to obtain structures at atomic resolution with around 600 movies. Moreover, D1R can form a stable complex with G protein without Nb35 (fig. S3, E to H).

The overall arrangement of the D1R–mini-G_s–Nb35 complex is largely similar to the previously determined GPCR–G_s protein complex (Fig. 1B). The high stability of the D1R-G_s complex may be attributed to the more extensive interaction interface between D1R and Gα than that between β1AR and Gα, including 2.5 helical turns of TM5 extension (fig. S2A). When compared to the β1AR-G_s complex, the entire Gαβγ heterotrimer in the D1R–G protein complex is rotated clockwise relative to the receptor (fig. S2, A and B). As a result, D312 at the Gβ subunit is in close proximity to $K339^{8.52}$ at helix 8 of D1R, leading to a close contact between Gβγ and D1R (fig. S2C). The TM5 extension in D1R likely accounts for the distinct orientation of the receptor and G protein from the β1AR-G_s complex (*25*). These findings suggest that the relative orientation of the receptor and G protein is very dynamic and may vary during the GPCR–G protein coupling cycle.

Plasticity of the ligand-binding site

When comparing our structure with two recently published structures of dopamine-bound D1R-G_s complex (*22*, *23*), we found that

the binding pose of dopamine varied among these structures (Fig. 1, C to E). While the binding modes of amine groups of dopamine that make salt bridge interaction with D103$^{3.32}$ (superscript corresponding to the Ballesteros-Weinstein numbering system) are almost identical, the catechol ring moves downward. The downward movement of the catechol ring in the binding pocket is accompanied by an upward shift of the entire Gαβγ and the second intracellular loop (ICL2), and the inward movement of TM5 (Fig. 1, C and D). In our structure, S198$^{5.42}$ makes strong hydrogen bonds with both hydroxyl groups of catechol, and the para hydroxyl group is more distant from and engages weaker hydrogen bond interactions with both S202$^{5.46}$ and T108$^{3.37}$ compared with the previously reported structure [Protein Data Bank (PDB) ID: 7CKZ] (Fig. 2A) (*23*). The downward movement of the catechol ring makes the para hydroxyl group close to the S202$^{5.46}$ and T108$^{3.37}$ in TM5 (Fig. 2A), allosterically leading to further inward movement of TM5 and the upward shift of ICL2 and G protein (Fig. 1, C and D). L190 at ECL2 moves in the same direction as dopamine, suggesting that it plays an important role in dopamine binding (Fig. 1E). The functionally equivalent residue of L190 in D2R is I184, which neighbors L190 and is located above dopamine when aligning two structures (fig. S2D). The different binding pose of the same ligand has also been observed between two D2R-G_i complex structures determined in micelle and lipid environment, respectively (*21*, *24*). Moreover, the conformations of the receptor–G protein interface and the agonist-binding pocket of D1R–mini-G_s–Nb35 in the GDP-bound state are almost identical to that in the nucleotide-free state (Fig. 2, B and C). However, in the absence of Nb35, the conformations of the receptor–G

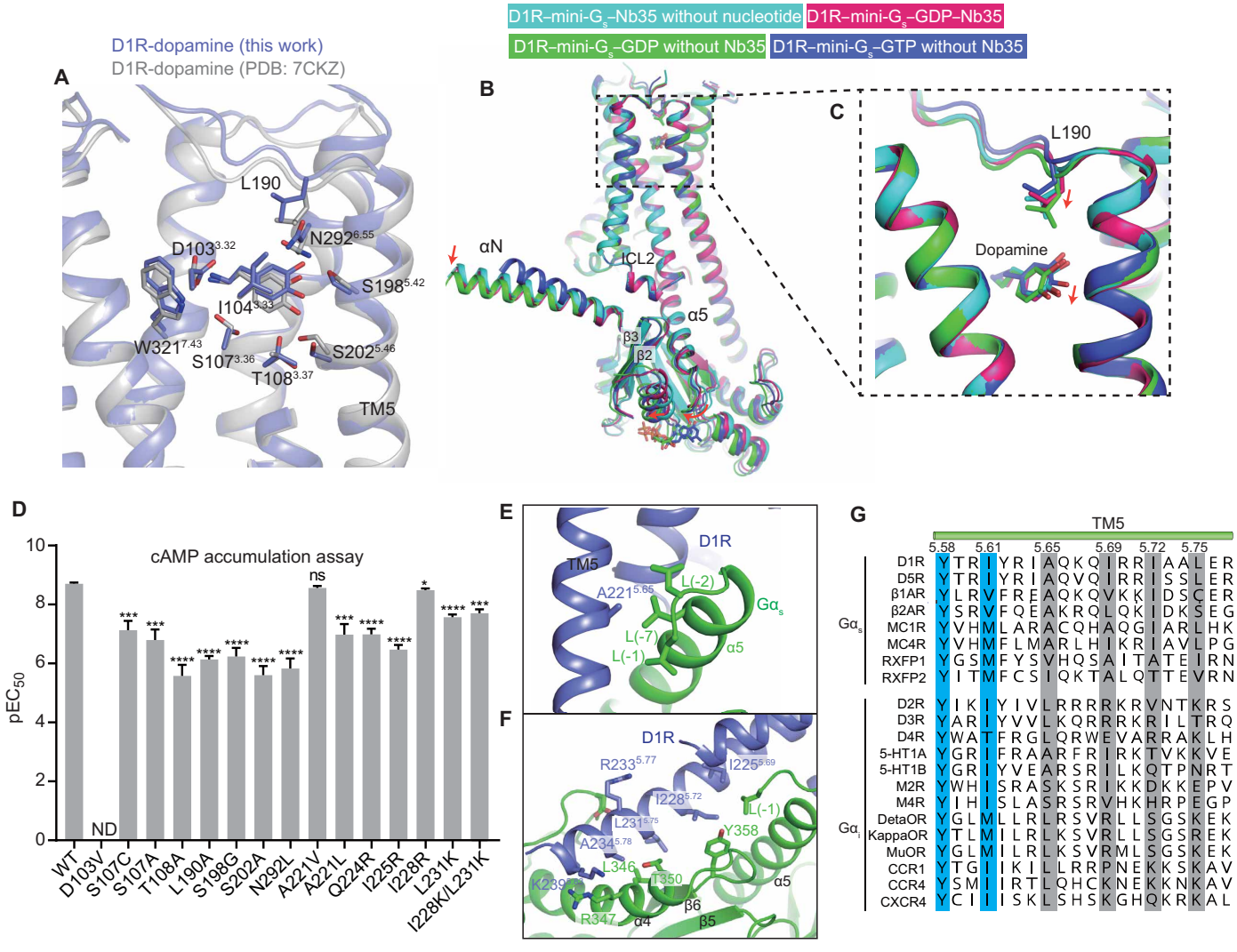

Fig. 2. Molecular determinants of the G protein selectivity by DRs. (**A**) Comparison of the binding pose of dopamine between our structure and the previously determined structure in the nucleotide-free state (PDB ID: 7CKZ). (**B**) Structural overlay of the D1R–mini-G_s–Nb35 complex without nucleotide bound (cyan), the GDP-bound D1R–mini-G_s–Nb35 (red), and the GDP- (green) and GTP-bound D1R–mini-G_s complex (blue) in the absence of Nb35 with D1R aligned. $G\beta_1\gamma_2$ and Nb35 are omitted for clarity. (**C**) Close-up views of the dopamine-binding pocket. (**D**) cAMP accumulation assay of D1R and D1R mutants activated by dopamine. *P* values were obtained by two-tailed Student's *t* test (*$P < 0.05$, **$P < 0.01$, ***$P < 0.001$, and ****$P < 0.0001$). ND, not determined due to no response; ns, not significant; WT, wild type. (**E**) A221$^{5.65}$ of the receptor engages hydrophobic interactions with L388, L393, and L394 at the α5 of Gα. (**F**) Detailed interactions between the TM5 extension and $G\alpha_s$. (**G**) Sequence alignment of the C-terminal part of TM5 from several G_s-coupled receptors and $G_{i/o}$-coupled receptors.

protein interface comprising ICL2 of the receptor and αN, α5, and the β2-β3 loop in the GDP-bound D1R–mini-G_s complex change, which results in a distinct binding pose of dopamine (Fig. 2, B and C), suggesting that Nb35 binding allosterically influences the conformation of the agonist-binding pocket. Consistent with the dynamic nature of GPCR signaling complexes (*10*), the ligand-binding pose in the GTP-bound D1R–mini-G_s complex is different from that in the GDP-bound complex, which is also attributed to the distinct conformation of the receptor–G protein interface (Fig. 2, B and C). Despite distinct binding poses of dopamine among different structures, a similar set of residues are involved in binding dopamine. The mutation of these residues such as D103$^{3.32}$, S107$^{3.36}$, T108$^{3.37}$, S198$^{5.42}$, S202$^{5.46}$, and L190^{ECL2} involved in binding dopamine significantly reduces potencies of dopamine in G_s coupling (Fig. 2D). Together, these structural observations further support the allosteric communication between G protein coupling and the agonist-binding pocket (*26*) and suggest that the conformation of the agonist-binding pocket varies depending on the conformation of the receptor–G protein interface that may change during the nucleotide-exchange process or through interaction with different downstream effectors.

The importance of the C-terminal part of TM5 in determining G protein specificity

The important role of ICL2, especially the hydrophobic residue at position 34.51, in determining G_s coupling selectivity has been well studied (*23*, *27*, *28*). In this work, we focus on the other regions that contribute to G protein selectivity of DRs. Most of the residues in TM3 and ICL2 involved in interactions with G_s are conserved in D2R (fig. S2, E and F). Notably, different residues are located at the C-terminal part of TM5 including the TM5 extension (Fig. 2, E to G). For example, A221$^{5.65}$ projects into a hydrophobic pocket formed by L(-7), L(-2), and L(-1) of α5 in $G\alpha_s$ (-1 represents the last residue of $G\alpha_s$) (Fig. 2E). While most G_s-coupled GPCRs prefer hydrophobic residues with smaller side chains including valine and alanine than leucine at the equivalent position of A221$^{5.65}$, G_i-coupled GPCRs can accommodate a variety of hydrophobic residues including leucine (Fig. 2G). The substitution of A221$^{5.65}$ to valine in D1R has little influence on the potency of dopamine, whereas substitution into leucine results in a significantly reduced potency (Fig. 2D). From a structural perspective, A221$^{5.65}$L mutation likely leads to steric clashes with the aforementioned hydrophobic pocket of α5 in $G\alpha_s$ because of their close distance. In addition, three hydrophobic residues including I225$^{5.69}$, I228$^{5.72}$, and L231$^{5.75}$ are located at the C terminus of TM5 and form extensive hydrophobic interactions with the Ras domain of $G\alpha_s$ (Fig. 2F). The three equivalent residues are hydrophobic residues in most G_s-coupled GPCRs, whereas at least one of the three equivalent residues in G_i-coupled GPCRs is a charged residue including lysine or arginine (Fig. 2G). Mutations of I225$^{5.69}$ into charge residues significantly impair the potency of dopamine, and the effect of I228$^{5.72}$ or L231$^{5.75}$ mutation is modest (Fig. 2D). The charged residues are particularly enriched in the C terminus of TM5 in G_i-coupled receptors and have been shown to be critical for G_i coupling (*29*). The important roles of A/V$^{5.65}$ and I225$^{5.69}$ in determining G_s selectivity were further verified using NanoBiT-based assay, which can directly assess effects of these mutations on interactions between D1R and G_s (fig. S2, G and H). Moreover, the coupling efficiency between D2R and G_s is markedly enhanced when the ICL3 in D2R including the A/V$^{5.65}\Phi^{5.69}$motif (Φ represents hydrophobic residues) is substituted by that in D1R (fig. S2I). Similarly, G_i-coupled α2-adrenergic receptor acquires the ability to activate G_s by replacing its ICL3 with that of the β2AR (*30*). Collectively, these results indicate that the A/V$^{5.65}\Phi^{5.69}$motif in TM5 is predominant in G_s-coupled receptors and plays an important role in determining G_s selectivity.

Structural basis for the GDP release upon G protein activation

Structures of GPCR–G protein complexes in the nucleotide-free state have shown that receptor binding to $G\alpha_s$ allosterically induces conformational changes of the α5-β6 loop, α1 and P loop of the nucleotide-binding site in Gα, and the separation of the AHD from the Ras domain, which are critical for receptor-mediated nucleotide release (*10*, *31*). However, it is yet to be determined the conformational steps of G protein activation and which regions are the major determinants for the initial release of GDP (*32*). To answer these questions, we sought to determine the structure of the D1R–mini-G protein complex in the presence of GDP. The overall structure of the GDP-bound D1R complex in the presence of Nb35 is similar to that of the D1R–mini-G protein complex in the nucleotide-free state (Fig. 3A and fig. S3, A to D). To rule out the possibility that Nb35 restricts the conformational change of the complex caused by GDP binding, we also determined the structure of the GDP-bound D1R–G protein complex without Nb35 (Fig. 3B and fig. S3, E to H). Both GDP and Mg^{2+} are present in the structure of the GDP-bound D1R–mini-G_s protein complex with Nb35 (Fig. 3A and fig. S4A) and the previously determined structure of the GDP-bound G_s heterotrimer (*17*), while Mg^{2+} is absent in the structure of the GDP-bound D1R–mini-G_s protein complex without Nb35 (Fig. 3B). The switch II of Gα undergoes large conformational change in the absence of Nb35, leading to a roughly 2-Å translational movement of the Gαβγ toward TM5, indicating that Nb35 affects the relative orientation of the receptor and G protein by influencing the conformation of the switch II (fig. S4, B and C). Since D223 in the switch II is involved in coordinating Mg^{2+} (fig. S4A), the conformational change of the switch II in the structure of the GDP-bound D1R complex without Nb35 likely disrupts their coordination (fig. S4C), accounting for its absence. Previous studies have shown that the removal of Mg^{2+} accelerates the GDP dissociation rate of guanosine triphosphatase (GTPase) (*33*). Therefore, receptor binding to G protein induces structural arrangement of the switch II, which disrupts contact of GDP with Mg^{2+} and is likely to be important for subsequent GDP release. Compared to the GDP-bound $G\alpha_s$ without receptor bound, GDP-bound $G\alpha_s$ in D1R-G complex shares common structural changes with the D1R-G complex in the nucleotide-free state in α5 of $G\alpha_s$, which undergoes rotational and translational movement (Fig. 3C). Structural studies of the GPCR–G protein complex in the nucleotide-free state suggest that ICL2 binding to the G protein induces the conformational change of the αN-β1 hinge region, which is propagated to the P loop through β1, and the conformational change of the P loop results in GDP release (*10*). However, our structure shows that the conformation of P loop and α1 involved in binding of the diphosphate of GDP almost remains in place upon receptor binding before GDP release, whereas V367 in the α5-β6 loop moves away from GDP by about 3 Å because of the structural rearrangement of α5 when engaged by the receptor (Fig. 3D). Since V367 sandwiches GDP with K293 in αG and is also involved in interaction between the AHD and the Ras domain (Fig. 3E), V367 movement weakens both the interaction between

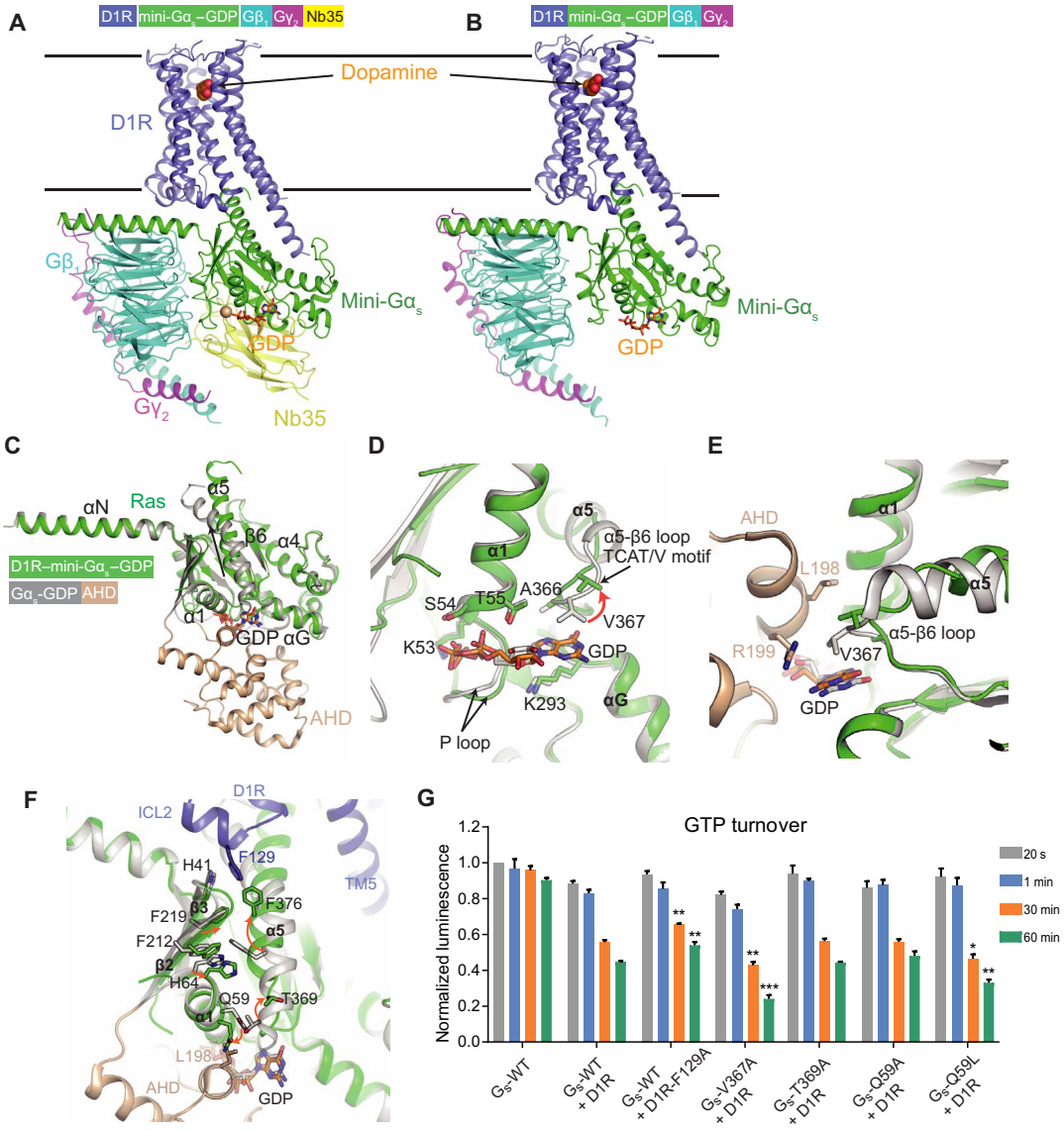

Fig. 3. Structural changes of Gα upon receptor engagement before GDP release. (**A**) Structure of dopamine-bound D1R–mini-G_s–Nb35 complex in the presence of GDP. GDP is shown as sticks and colored in orange. The same color scheme as Fig. 1B was used for proteins. (**B**) Structure of the dopamine-bound D1R–mini-G_s complex without Nb35 in the presence of GDP. (**C**) Comparison of the structures of receptor-free $G\alpha_s$ (PDB ID: 6EG8) and D1R-bound $G\alpha_s$ (green) in the presence of GDP. D1R and Gβγ were omitted for clarity. The Ras domain and AHD in free $G\alpha_s$ are colored in gray and wheat, respectively. (**D**) The receptor induces the conformational change of α5, which subsequently leads to the upward movement of V367 at the α5-β6 loop. (**E**) Structural change of V367 influences the interaction between AHD and Ras. (**F**) The conformational change of α5 leads to structural arrangement of α1, which disrupts the interaction between the AHD and the Ras domain. (**G**) GTP turnover experiments of wild-type G_s or mutants induced by D1R receptor. All experiments are repeated in three independent times. Significance is calculated by comparing the wild type and mutants at the same time point using two-tailed Student's *t* test.

Gα and GDP and the interaction between the AHD and the Ras domain. Previous mutagenesis studies have shown that insertion of a flexible linker including five glycine residues but not a rigid α-helical segment between TCAT/V motif (T/V corresponds to V367 in $G\alpha_s$) and α5 blocks the G protein activation by GPCRs (*34*). This flexible linker absorbs the structural change of α5 induced by receptor binding and disrupts the conformational change of V367, which eventually prevents GDP release. To further support our structural observations, we performed in vitro GTP turnover assay using the purified D1R and G_s heterotrimer. As expected, D1R catalyzes rapid GDP/GTP exchange on Gα subunits compared to the G_s heterotrimer alone, and the GTP turnover rate of D1R for the V367A mutant of $G\alpha_s$ is substantially increased (Fig. 3G), underscoring the important role of V367 in receptor-induced GDP release. Moreover, another noticeable feature in the structure of the GDP-bound complex is the rotational movement of α1 in Gα (Fig. 3F), which possibly plays a key role in the separation of the AHD domain from the Ras domain. In the GDP-bound Gα without receptor bound, F376 of α5 engages aromatic interactions with H64 of α1, F212 of β2, and F219 of β3, and Q59 of α1 makes hydrogen bonds with T369 of α5 (Fig. 3F). When engaged by $F129^{34.51}$ in ICL2 of D1R, F376 in α5 undergoes translational and rotational movement, which disrupts

its aromatic interactions with nearby residues and the hydrogen bond between Q59 and T369, leading to the translational movement of F212 and F219 and the rotational movement of H64 and Q59 in α1 (Fig. 3F) (*35*). The movement of Q59 causes a steric clash with L198 in AHD, thus destabilizing the AHD-Ras domain interface. The functional importance of $F^{34.51}$ in ICL2 is shown by a mutation to alanine that significantly reduces the GTP turnover rate of D1R (Fig. 3G) and almost abrogates GDP release induced by β2AR (*6*). Besides, the slower GTP turnover rate of the family B glucagon receptor could be attributed to the absence of strong hydrophobic interactions between the residue in ICL2 analogous to $F^{34.51}$ in D1R and β2AR, and $G\alpha_s$ (*36*). Furthermore, the steric effect

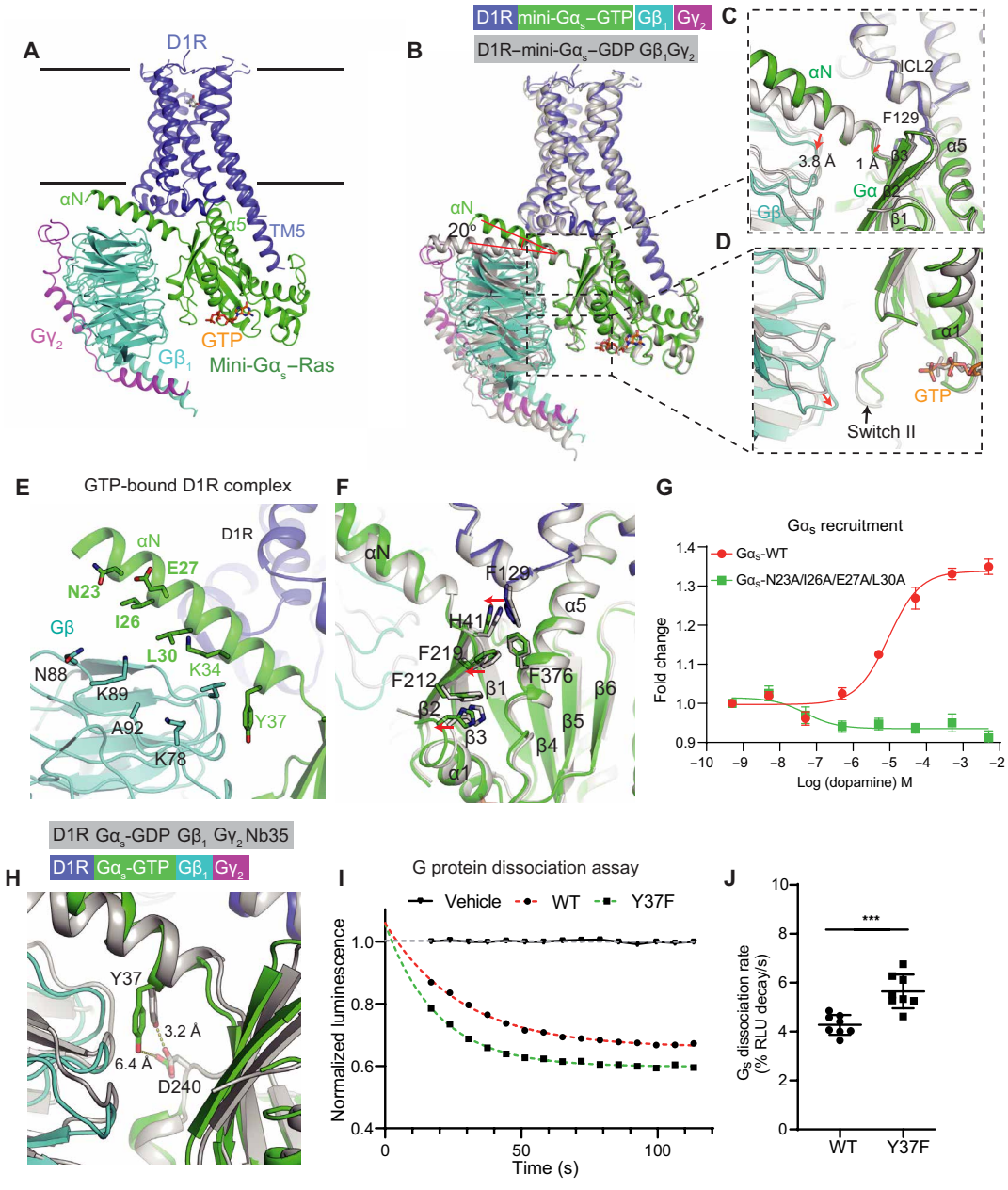

Fig. 4. Structural changes of Gα upon receptor engagement after the exchange of GDP for GTP. (**A**) Overall structure of the GTP-bound D1R–mini-G_s complex with Nb35 dislodged. (**B**) Structural overlay of the GDP and GTP-bound D1R–mini-G_s complex without Nb35 bound. Receptors are aligned. The αN is tilted 20° toward the receptor upon GTP binding. (**C** and **D**) Close-up view of conformational changes of the switch II, Gβγ, and the αN-β1 hinge induced by GTP binding. (**E**) Interface of αN-Gβγ in the GTP-bound D1R–G protein complex. (**F**) Conformational differences between the GDP- and GTP-bound D1R complex. (**G**) Disruption of the αN-Gβγ interface abolishes G protein recruitment, as revealed by NanoBiT G protein recruitment assay using D1R-SmBiT and $G\alpha_s$-LgBiT. (**H**) GTP binding disrupts the hydrogen bond between Y37 and D240 in $G\alpha_s$. (**I**) G protein dissociation curve of $G\alpha_s$ wild type and Y37F mutant at a saturated concentration of dopamine measured by NanoBiT dissociation assay. (**J**) Significance analysis of G_s dissociation rate of $G\alpha_s$ wild type and Y37F mutant from eight independent experiments by two-tailed Student's *t* test. RLU, relative light unit.

of Q59 is supported by mutagenesis studies showing that the GTP turnover rate of D1R in the Q59L mutant of $G\alpha_s$ but not the Q59A mutant is markedly increased. This can be explained by the fact that although both Q59A and Q59L mutants disrupt the hydrogen bond between Q59 in α1 and T369 in α5, alanine fails to mimic the steric effect of Q59 because of its smaller side chain. Moreover, T369A mutation in $G\alpha_s$ has little effect on the GTP turnover rate of D1R (Fig. 3G), whereas the equivalent mutation, T329A in $G\alpha_i$, causes a notable increase in receptor-independent GDP release (*37*). Together, our results indicate that receptor binding to G_s protein induces the rotational movement of Q59 in α1 that causes the separation of AHD from Ras and the conformational change of V367 in the α5-β6 loop that weakens GDP binding, both of which are critical for G protein activation. Following GDP release before GTP binding, the α1 and α5-β6 loop move further toward the TM5 of the receptor, while the α5 remains in place (fig. S4D). The conformational dynamics of α1 and the α5-β6 loop during G protein activation are demonstrated by HDX-MS results, showing that receptor binding induces an increase in HDX in these regions (*6*).

Structure of GTP-bound D1R–G protein complex

Although the structure of GTP-bound Gα has provided insight into mechanisms of the GTP-dependent dissociation of Gα from Gβγ (*38*), it remains unclear how GTP triggers the dissociation of G proteins from receptors. The mini-$G\alpha_s$ we used for structure determination includes an I372A mutation at α5 that makes the receptor–G protein complex resistant to GTP-mediated dissociation (*39*). We speculate that we may capture a GTP-bound intermediate state before the receptor–G protein dissociation. D1R can form a stable complex with G protein in the presence of GTP from the two-dimensional (2D) classification (fig. S5A). We were able to obtain two different structures, one with Nb35 occupied and one with Nb35 dislodged after 3D classification (Fig. 4A and fig. S5, B to H). The EM density for the triphosphate group of GTP is relatively poor, likely due to the low resolution and high flexibility of GTP (fig. S5H). However, we can conclude that the switch II in the GTP-bound D1R–mini-G_s is closer to the GTP than that in the GDP-bound D1R–mini-G_s complex (Fig. 4, B to D). Therefore, the γ-phosphate of GTP potentially interacts with the switch II of Ras domain and leads to its structural arrangement, which subsequently expels the Nb35 (Fig. 4D). The conformational change of the switch II arising from GTP binding causes the movement of Gβγ by about 3.8 Å (Fig. 4C). In contrast, the αN-β1 hinge in Gα moves by only 1 Å because of strong hydrophobic interactions between $F129^{34.51}$ in ICL2 of D1R and residues in the αN-β1 hinge, the β2-β3 loop, and α5, which limits the movement of the αN-β1 hinge. As a result, the imbalanced movement of Gβγ and the αN-β1 hinge in Gα disrupts the interface of αN and Gβγ, such that the αN helix of Gα in the GTP-bound D1R-G complex is tilted around 20° toward the receptor compared to that

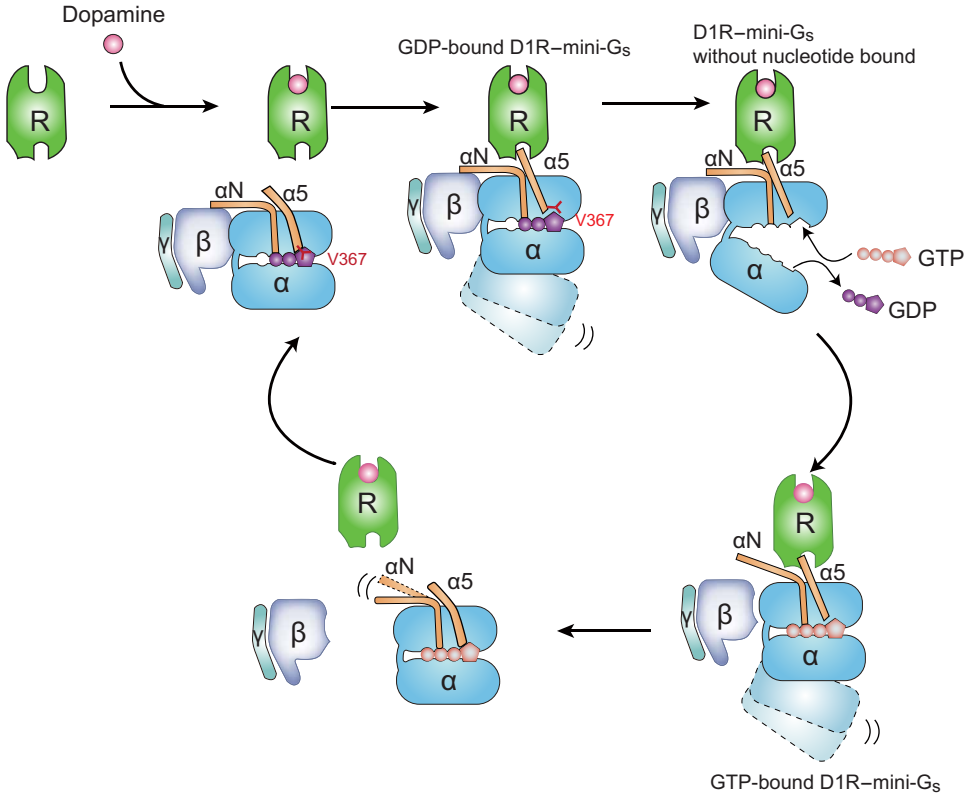

Fig. 5. A model for G_s activation by D1R. G protein engagement by the receptor causes the rotational and translational movement of α5, which leads to the upward movement of V367 and structural rearrangement of α1. These conformation changes together cause the separation of the AHD and the Ras domain and weaken the GDP-binding affinity, leading to GDP release. Subsequent GTP binding results in the conformational change of αN and switch II, accounting for the dissociation of Gβγ from Gα.

in the D1R-G complex in the nucleotide-free or GDP-bound state (Fig. 4B). In contrast, no conformational change of αN is observed in the structure of the GTP-bound D1R–mini-G_s complex in the presence of Nb35 (fig. S5G) and in all other structures of the D1R–mini-G_s complex with Nb35 bound (Figs. 1B and 3, A and B), suggesting that Nb35 restricts the conformational change of αN by stabilizing the conformation of the switch II. The movement of αN results in smaller interaction interface between Gα and Gβγ in the GTP-bound D1R–G protein complex (Fig. 4E). Moreover, GTP binding causes the displacement of H41 in the αN-β1 hinge and F219 in β3 away from α5, enlarging the hydrophobic pocket where F129 is inserted and weakening interactions between Gα and D1R (Fig. 4F). The movement of αN observed in our structure is consistent with results of fluorescence labeling experiments and HDX-MS, showing that αN underwent large conformational change upon interaction with receptors and GTP (*6*, *28*, *40*, *41*). However, the conformational change of αN was not captured in previous structural studies of GPCR–G protein complexes because of the absence of nucleotide and the use of Nb35 and scFV16 that stabilize the conformation of the switch II loop and the αN-Gβγ interface, respectively (*5*, *13*). The recruitment of $G\alpha_s$ to D1R is completely abolished, when N23, I26, E27, and L30 in αN are mutated to alanine to disrupt the αN and Gβγ interface (Fig. 4G). Previous studies have shown that although αN truncations of Gα reduce the binding affinity between Gα and Gβγ, the truncated Gα could still interact with Gβγ (*42*). These data suggest that Gβγ contributes to the initial G protein coupling to the receptor partially by stabilizing the conformation of αN. Direct interactions between Gβγ and receptors that are observed in many structures of GPCR–G protein complexes are involved in G protein coupling as well (*11*). To further support our structural findings, we analyzed the effect of mutations that favor a GTP-bound conformational state on G_s dissociation kinetics using NanoBiT-based G protein dissociation assay. In the GDP-bound D1R complex, Y37 in αN makes a hydrogen bond with D240 in Gα, while in the GTP-bound D1R complex, the movement of αN disrupts this hydrogen bond (Fig. 4H). As expected, Y37F mutation that disrupts its hydrogen bond with D240 and favors the GTP-bound state has little influence on G_s recruitment (fig. S6A) but leads to a faster G_s dissociation rate catalyzed by D1R (Fig. 4, I and J, and fig. S6B). In conclusion, the conformational changes of the switch II region and αN serve as molecular basis for the GTP-dependent dissociation of Gβγ from Gα and of G protein from receptors.

In summary, these structures captured several intermediate states adopted by mini-$G\alpha_s$ coupled to D1R and provided a framework for understanding key aspects of GPCR–G protein coupling events, including initial G protein engagement by the receptor, receptor-mediated GDP release, and GTP-dependent complex dissociation (Fig. 5 and movie S1). As validated by mutagenesis studies, the fundamental properties found here likely apply to the full-length $G\alpha_s$ proteins and other GPCRs. The structure of the GDP-bound D1R–G protein complex reveals conformational steps of G protein activation by GPCR and critical regions for initial release of GDP. AHD domain is invisible in most structures of GPCR–G protein complexes in the nucleotide-free state because of its high flexibility after the separation of AHD from Ras that occurs at the early stage of coupling events, even without receptor binding (*9*). Therefore, the conformational state of the GDP-bound complex captured here using mini-G protein that lacks the AHD domain may represent an intermediate state of G protein upon receptor binding after AHD domain opening before GDP release but not the precoupled state where the α5 helix likely adopts a different configuration from our structures (*17*). Moreover, structural findings in the GTP-bound D1R complex highlight the important role of αN in G protein recruitment and GTP-dependent dissociation of G protein from the receptor. Together, our studies further advance our mechanistic understanding of G protein activation by GPCRs.

MATERIALS AND METHODS

Cloning and expression of D1R–mini-G_s fusion protein

The human wild-type full-length D1R gene was cloned into a pcDNA3.1(+) vector (Thermo Fisher Scientific) with the signal peptide substituted by that of hemagglutinin (HA) and expressed with an N-terminal Flag tag and a C-terminal mini-$G\alpha_s$399 fusion protein. 3C protease site was introduced between D1R and mini-$G\alpha_s$ protein. Plasmids expressing fusion protein were transiently transfected into Expi293F cells (Thermo Fisher Scientific) using polyethylenimine (Polysciences) when cells reached a density of 1.5 million/ml. Sodium butyrate (5 mM) and 3 mM valproic acid were added into the culture 18 hours after transfection, and cells were shaken for another 30 hours before harvesting by centrifugation at 1000*g* for 10 min.

Cells were lysed in hypotonic buffer [25 mM Hepes-NaOH (pH 7.6), 50 mM NaCl, and 100 μM dopamine] using a glass dounce tissue grinder. Membrane was pelleted by centrifugation at 60,000*g* at 4°C for 1 hour and homogenized in solubilization buffer containing 25 mM Hepes (pH 7.6), 150 mM NaCl, 0.5% lauryl maltose neopentyl glycol (LMNG) (Anatrace), 0.1% cholesteryl hemisuccinate (CHS; Anatrace), and 10 μM dopamine (Sigma-Aldrich) using dounce. The sample was mixed for 2 hours at 4°C. After centrifugation to remove the debris, the supernatant supplemented with 2 mM $CaCl_2$ was loaded onto anti-Flag antibody affinity resin by gravity flow. The resin was washed extensively with at least 10 column volumes of wash buffer containing 25 mM Hepes (pH 7.6), 150 mM NaCl, 0.01% LMNG, 0.002% CHS, 2 mM $CaCl_2$, 10 mM $MgCl_2$, 2 mM KCl, 2 mM adenosine triphosphate, and 10 μM dopamine. The receptor was eluted in elution buffer [25 mM Hepes, 150 mM NaCl, 0.01% LMNG, 0.002% CHS, 5 mM EDTA, Flag peptide (0.1 mg/ml), and 10 μM dopamine]. The protein sample was concentrated by ultrafiltration and incubated with peptide *N*-glycosidase F (New England Biolabs) overnight.

Complex assembly

His6-tagged human $G\beta_1$ and $G\gamma_2$ with C68S mutation was expressed in insect cell using the Bac-to-Bac baculovirus expression system (Invitrogen) and purified as previously described (*43*). Nb35 was expressed in *Escherichia coli strain* BL21 (DE3) and purified as previously reported (*5*). For the D1R–mini-$G\alpha_s$–$G\beta_1\gamma_2$–Nb35 complex assembly and purification, purified D1R–mini-$G\alpha_s$ fusion protein, $G\beta_1\gamma_2$, and Nb35 were mixed in a 1:1.2:1.2 molar ratio and added with 2 mM $MgCl_2$ and apyrase. Nb35 was not included for the D1R–mini-G_s–$G\beta_1\gamma_2$ complex assembly. After incubation at 4°C overnight, the protein complex was further purified with Superose 6 10/300 to remove the excess $G\beta_1\gamma_2$ and Nb35 in the buffer containing 25 mM Hepes (pH 7.6), 150 mM NaCl, 0.01% LMNG, 0.002% CHS, and 10 μM dopamine. The complex peak was pooled and concentrated to 4 mg/ml for cryo-EM analysis.

Cryo-EM sample preparation and data collection

Purified complex (3.0 μl) was applied to glow-charged 300-mesh holey carbon grid (Quantifoil Au R1.2/1.3). Grids were blotted for 3.0 to 4.0 s at a blotting force of 4 and vitrified using a Vitrobot MarkIV (Thermo fisher Scientific), with chamber maintained at 8°C and 100% humidity. For the nucleotide-bound complex, 1 mM GDP or GTP and 2 mM $MgCl_2$ were added to the protein sample before grid preparation using the same condition as above. Cryo-EM movies were collected on a Titan Krios (Thermo Fisher Scientific) operated at 300 kV and equipped with a BioQuantum GIF/K3 direct electron detector (Gatan) in a superresolution mode at a nominal magnification of ×64,000. Each movie stack was collected as 32 frames with a total dose of 50 $e^-/Å^2$ for 2.56 s. Cryo-EM data collection parameters for all protein samples are summarized in table S1.

Data processing

For the nucleotide-free D1R–mini-$G\alpha_s$–$G\beta_1\gamma_2$–Nb35 complex, a total of 2320 movie stacks were collected and subjected to motion correction with 2× binned to a pixel size of 1.087 Å using MotionCor2 (*44*). Contrast transfer function (CTF) estimation was performed using patch-based CTF estimation in cryoSPARC (*45*). A total of 3,876,379 particles were autopicked using the Blob picker in cryoSPARC. These particles were split into three groups extracted in a 180-pixel box and subjected to 2D classification in cryoSPARC. Particles with good 2D class average were combined and run through the next round of 2D classification. Ab initio reconstruction with five classes using 1,045,088 particles was performed in cryoSPARC and subjected to heterogeneous refinement. Particles from classes with clear secondary structure were selected and run through another round of Ab initio reconstruction with six classes and subsequent heterogeneous refinement. Two classes with high-resolution and clear transmembrane helices were combined and applied to nonuniform refinement in cryoSPARC, resulting in a map with a global resolution of 3.1 Å.

For the GDP-bound D1R–mini-$G\alpha_s$–$G\beta_1\gamma_2$–Nb35 complex, a total of 601 movies were collected, and similar procedure was performed as above. In brief, ab initio reconstructions with five classes using 317,029 particles yield two good classes with clear secondary structure, accounting for 65.3% of total particles. The two classes were combined and subjected to nonuniform refinement, yielding a map with a global resolution of 3.1 Å.

For the GDP-bound D1R–mini-$G\alpha_s$–$G\beta_1\gamma_2$ complex, 448,009 particles with good 2D class average from 681 movies were extracted in a 180-pixel box in cryoSPARC and exported into RELION format using csparc2star.py script from UCSF PyEM package (*46*). These particles were used for 3D classification in RELION (*47*). One class accounting for 46.3% particles showing a well-defined structure was selected and imported back to cryoSPARC and run through nonuniform refinement to yield a map at 3.5-Å resolution.

For the GTP-bound D1R–mini-$G\alpha_s$–$G\beta_1\gamma_2$–Nb35 complex, particles from 1242 movies were subjected to two rounds of 2D classification by cryoSPARC and one round of 2D classification by RELION, yielding 628,083 good particles. 3D classification was performed in RELION, resulting in one good class accounting for 49.5% particles. The next round of 3D classification yielded two classes with clear transmembrane helices, one with Nb35 occupied and one with Nb35 dislodged. For the complex without Nb35, we performed 3D refinement with mask excluding micelle. For the complex with Nb35, particles were imported to cryoSPARC and run through nonuniform refinement to yield a map at 3.6-Å resolution. Resolutions are reported on the basis of the gold standard Fourier shell correlation (FSC) at the 0.143 criterion. All cryo-EM maps were postprocessed by DeepEMhancer to improve their interpretability (*48*).

Model building

A homology model of D1R was generated using SWISS-MODEL server (*49*) with activated structure of β1AR (PDB ID: 7JJO) as a template and was docked into the EM density map along with mini-G_s–Nb35 structure in Chimera (*50*). The model was manually built in COOT (*51*) and refined with Phenix (*52*). Initial restraints for dopamine, GDP, and GTP were generated using eLBOW in Phenix. If the side chain density is too poor to assign a conformation, then we temporarily chop the side chain while keeping the sequence information. Model was validated using MolProbity (*53*) and EMRinger (*54*). Model-to-map FSC curves were calculated in Phenix. Structure figures are prepared with PyMOL and Chimera. Detailed structure statistics are summarized in table S1.

Cyclic adenosine 3′,5′-monophosphate accumulation assay

The human full-length D1R gene was cloned into pcDNA3.1(+) vector with an N-terminal flag tag. All point mutations are introduced by the QuikChange method. Human embryonic kidney (HEK) 293 cells stably expressing the GloSensor biosensor (Promega) were plated into a six-well plate in Dulbecco's modified Eagle's medium (DMEM; Gibco) supplemented with 10% fetal bovine serum (FBS; Gibco), penicillin, and streptomycin and transfected with wild-type or mutated D1R plasmids using polyethylenimine. After transfection, cells were incubated at 37°C with 5% CO_2 for 24 hours. Then, cells were collected and seeded in a tissue culture–treated, white, and clear-bottom 96-well plate. After incubation for another 24 hours, culture medium was removed, and equilibration medium (CO_2-independent medium, 10% FBS, and 1% D-luciferin) was added to each well. Cells were incubated at room temperature for 2 hours before treatment with increasing concentration of dopamine. The luminescence signal was measured in 10 min after the addition of dopamine and plotted as a function of dopamine concentration using nonlinear regression with GraphPad Prism 8 (GraphPad Software). EC_{50} (median effective concentration) indicates the concentration of ligand, which can produce 50% of the maximum luminescence signal. Each measurement was repeated in three independent experiments, each in triplicate. Significance was calculated by two-tailed Student's *t* test.

NanoBiT G_s dissociation assay

NanoBiT-based G_s dissociation assay was performed as previously described (*55*). The large fragment (LgBiT) and small fragment (SmBiT) that comprise a catalytically active luciferase were fused to the AHD domain of $G\alpha_s$ ($G\alpha_s$-LgBiT) and the N terminus of $G\gamma_2$ with a C68S mutation (SmBiT-Gγ2), respectively. HEK293T cells were seeded in a six-well plate using the same DMEM medium as above. D1R (200 ng), 100 ng of $G\alpha_s$-LgBiT, 500 ng of $G\beta_1$, 500 ng of SmBiT-$G\gamma_2$, and 100 ng of RIC8B were transfected into cells using polyethylenimine solution when cells reach 80% confluency. After 1 day of incubation, cells were washed with Dulbecco's phosphate-buffered saline and suspended in 3 ml of Hanks' balanced salt solution (HBSS) reaction buffer [HBSS supplemented with 0.01% BSA and 5 mM Hepes (pH 7.4)]. Coelenterazine was added to cell suspensions at a final concentration of 10 μM. Cells were seeded into a 96-well plate with 1×10^5 cells per well in 95 μl of HBSS reaction buffer. After

incubation at room temperature for 1 hour, baseline luminescence signals were measured using a luminescent microplate reader (Tecan, Spark). Five microliters of increasing concentration of dopamine (20× of final concentrations) diluted in HBSS reaction buffer was added to cells. Luminescence signals were measured in 3 to 5 min after ligand addition and normalized over baseline signal. The resulting fold changes are plotted as a function of concentrations of dopamine using a three-parameter sigmoidal concentration-response model built in Prism 8.0.

To calculate the dissociation speed at a concentration of dopamine producing saturated luminescence, the plate was immediately read at an interval of 6.8 s with an accumulation time of 0.5 s per read for 2 min following ligand addition. The luminescence signal was normalized to the baseline count. The normalized signal was fitted using one-phase dissociation model built in Prism 8.0. The dissociation speed K represented decreased luminescence per second.

NanoBiT G protein recruitment assay

For monitoring recruitment of $G\beta_1\gamma_2$, LgBiT and SmBiT were fused with the C terminus of D1R and the N terminus of $G\beta_1$ to yield D1R-LgBiT and SmBiT-$G\beta_1$ fusion proteins, respectively. Plasmid mixtures containing 200 ng of D1R-LgBiT, 100 ng of $G\alpha_s$, 500 ng of SmBiT-$G\beta_1$, 500 ng of $G\gamma_2$C68S, and 100 ng of RIC8B were transfected into HEK293T cells.

For directly monitoring recruitment of Gα, D1R-SmBiT containing D1R fused to SmBiT at its C terminus, $G\alpha_s$-LgBiT, $G\beta_1$, and $G\gamma_2$C68S were expressed with RIC8B in HEK293T cells using the same amount of plasmids as above. For mini-G_s recruitment assay, LgBiT–mini-$G\alpha_s$ consisting of mini-$G\alpha_s$399 (*15*) fused to LgBiT at its N terminus and D1R-SmBiT were coexpressed in HEK293T cells.

Similar procedures were performed as G protein dissociation assay. In brief, luminescence signals were measured in 3 to 5 min following the addition of increasing concentration of dopamine and normalized to baseline signal. The resulting fold changes were fitted by nonlinear regression using Prism.

GTP turnover assay

Human $G\alpha_s$ and its mutants used for the assay were expressed and purified from bacteria. $G\alpha_s$ (residues 7 to 394) was cloned into pET28a vector with an N-terminal His_6-SUMO-Flag tag. All point mutations in Gα were introduced using the QuikChange method. The plasmids were transformed into *E. coli* BL21 (DE3). The transformed bacteria were cultured in LB medium supplemented with kanamycin (50 μg/ml) at 37°C to an OD_{600} (optical density at 600 nm) value of 0.8 and were shaken at 25°C overnight following addition of 500 μM β-D-thiogalactopyranoside. After harvesting by centrifugation, cells were resuspended in lysis buffer [20 mM Hepes (pH 7.4), 300 mM NaCl, 2 mM $MgCl_2$, 10 μM GDP, 100 μM tris(2-carboxyethyl) phosphine (TCEP), and 15% glycerol) and lysed by sonication. Cell lysate was supplemented with Ubl-specific protease 1 (ULP1) to cleave His_6-SUMO tag, and flag-tagged $G\alpha_s$ was purified by M1 Flag affinity chromatography. Resin was washed with wash buffer containing 20 mM Hepes (pH 7.4), 100 mM NaCl, 2 mM $MgCl_2$, 2 mM $CaCl_2$, 10 μM GDP, and 100 μM TCEP, and proteins were eluted with elution buffer containing 20 mM Hepes (pH 7.4), 100 mM NaCl, 2 mM $MgCl_2$, 10 μM GDP, 100 μM TCEP, 5 mM EDTA, and Flag peptide (0.1 mg/ml). The eluted $G\alpha_s$ was incubated with 1.2-fold molar excess of $G\beta_1\gamma_2$ at 4°C for 1 hour. The assembled complex was further purified by size exclusion chromatography on a Superdex 200 10/300 increase column in buffer containing 20 mM Hepes (pH 7.4), 100 mM NaCl, 5 mM $MgCl_2$, 0.03% *n*-dodecyl-β-D-maltopyranoside (DDM), 10 μM GDP, and 100 μM TCEP. Peak fractions were pooled and concentrated to 1 mg/ml for GTP turnover assay.

The GTP turnover assay was performed as previously described (*36*). DDM-solubilized D1R (1 μM) was incubated with 200 μM dopamine in buffer containing 20 mM Hepes (pH 7.4), 100 mM NaCl, and 0.03% DDM for 60 min at room temperature. A final concentration of 10 μM GTP was added into D1R before mixing D1R with 500 nM G protein in buffer containing 20 mM Hepes, 100 mM NaCl, 20 mM $MgCl_2$, 0.03% DDM, 200 μM TCEP, and 1 μM GDP. After incubation for an indicated time, reconstituted GTPase-Glo reagent made according to the manufacturer's protocol (Promega) was added to the reaction and incubated for 30 min at room temperature. Luminescence was measured in 5 min following the addition of detection reagent at room temperature using Tecan Spark. The data were normalized to the initial count of G_s without the addition of receptor and then analyzed using Prism 8. Significance was obtained by two-tailed Student's *t* test with Welch's correction.

SUPPLEMENTARY MATERIALS

Supplementary material for this article is available at https://science.org/doi/10.1126/sciadv.abo4158

View/request a protocol for this paper from *Bio-protocol*.

REFERENCES AND NOTES

1. R. J. Lefkowitz, Seven transmembrane receptors: Something old, something new. *Acta Physiol (Oxf.)* **190**, 9–19 (2007).
2. R. Fredriksson, M. C. Lagerstrom, L. G. Lundin, H. B. Schioth, The G-protein-coupled receptors in the human genome form five main families. Phylogenetic analysis, paralogon groups, and fingerprints. *Mol. Pharmacol.* **63**, 1256–1272 (2003).
3. A. G. Gilman, G proteins: Transducers of receptor-generated signals. *Annu. Rev. Biochem.* **56**, 615–649 (1987).
4. T. M. Wilkie, D. J. Gilbert, A. S. Olsen, X.–. N. Chen, T. T. Amatruda, J. R. Korenberg, B. J. Trask, P. de Jong, R. R. Reed, M. I. Simon, N. A. Jenkins, N. G. Copeland, Evolution of the mammalian G protein alpha subunit multigene family. *Nat. Genet.* **1**, 85–91 (1992).
5. S. G. Rasmussen, B. T. De Vree, Y. Zou, A. C. Kruse, K. Y. Chung, T. S. Kobilka, F. S. Thian, P. S. Chae, E. Pardon, D. Calinski, J. M. Mathiesen, S. T. A. Shah, J. A. Lyons, M. Caffrey, S. H. Gellman, J. Steyaert, G. Skiniotis, W. I. Weis, R. K. Sunahara, B. K. Kobilka, Crystal structure of the β2 adrenergic receptor-Gs protein complex. *Nature* **477**, 549–555 (2011).
6. Y. Du, N. M. Duc, S. G. F. Rasmussen, D. Hilger, X. Kubiak, L. Wang, J. Bohon, H. R. Kim, M. Wegrecki, A. Asuru, K. M. Jeong, J. Lee, M. R. Chance, D. T. Lodowski, B. K. Kobilka, K. Y. Chung, Assembly of a GPCR-G protein complex. *Cell* **177**, 1232–1242.e11 (2019).
7. K. Y. Chung, S. G. F. Rasmussen, T. Liu, S. Li, B. T. DeVree, P. S. Chae, D. Calinski, B. K. Kobilka, V. L. Woods Jr., R. K. Sunahara, Conformational changes in the G protein Gs induced by the β2 adrenergic receptor. *Nature* **477**, 611–615 (2011).
8. N. Van Eps, A. M. Preininger, N. Alexander, A. I. Kaya, S. Meier, J. Meiler, H. E. Hamm, W. L. Hubbell, Interaction of a G protein with an activated receptor opens the interdomain interface in the alpha subunit. *Proc. Natl. Acad. Sci. U.S.A.* **108**, 9420–9424 (2011).
9. R. O. Dror, T. J. Mildorf, D. Hilger, A. Manglik, D. W. Borhani, D. H. Arlow, A. Philippsen, N. Villanueva, Z. Yang, M. T. Lerch, W. L. Hubbell, B. K. Kobilka, R. K. Sunahara, D. E. Shaw, SIGNAL TRANSDUCTION. Structural basis for nucleotide exchange in heterotrimeric G proteins. *Science* **348**, 1361–1365 (2015).
10. D. Hilger, M. Masureel, B. K. Kobilka, Structure and dynamics of GPCR signaling complexes. *Nat. Struct. Mol. Biol.* **25**, 4–12 (2018).
11. J. Garcia-Nafria, C. G. Tate, Cryo-EM structures of GPCRs coupled to G_s, G_i and G_o. *Mol. Cell Endocrinol.* **488**, 1–13 (2019).
12. J. Wang, T. Hua, Z. J. Liu, Structural features of activated GPCR signaling complexes. *Curr. Opin. Struct. Biol.* **63**, 82–89 (2020).
13. S. Maeda, A. Koehl, H. Matile, H. Hu, D. Hilger, G. F. X. Schertler, A. Manglik, G. Skiniotis, R. J. P. Dawson, B. K. Kobilka, Development of an antibody fragment that stabilizes GPCR/G-protein complexes. *Nat. Commun.* **9**, 3712 (2018).
14. A. Manglik, B. K. Kobilka, J. Steyaert, Nanobodies to study G protein-coupled receptor structure and function. *Annu. Rev. Pharmacol. Toxicol.* **57**, 19–37 (2017).

15. R. Nehmé, B. Carpenter, A. Singhal, A. Strege, P. C. Edwards, C. F. White, H. Du, R. Grisshammer, C. G. Tate, Mini-G proteins: Novel tools for studying GPCRs in their active conformation. *PLOS ONE* **12**, e0175642 (2017).
16. Y. Cheng, Single-particle cryo-EM at crystallographic resolution. *Cell* **161**, 450–457 (2015).
17. X. Liu, X. Xu, D. Hilger, P. Aschauer, J. K. S. Tiemann, Y. du, H. Liu, K. Hirata, X. Sun, R. Guixà-González, J. M. Mathiesen, P. W. Hildebrand, B. K. Kobilka, Structural insights into the process of GPCR-G protein complex formation. *Cell* **177**, 1243–1251.e12 (2019).
18. J. M. Beaulieu, R. R. Gainetdinov, The physiology, signaling, and pharmacology of dopamine receptors. *Pharmacol. Rev.* **63**, 182–217 (2011).
19. S. C. Sealfon, C. W. Olanow, Dopamine receptors: From structure to behavior. *Trends Neurosci.* **23**, S34–S40 (2000).
20. D. Vallone, R. Picetti, E. Borrelli, Structure and function of dopamine receptors. *Neurosci. Biobehav. Rev.* **24**, 125–132 (2000).
21. Y. Zhuang, P. Xu, C. Mao, L. Wang, B. Krumm, X. E. Zhou, S. Huang, H. Liu, X. Cheng, X. P. Huang, D. D. Shen, T. Xu, Y. F. Liu, Y. Wang, J. Guo, Y. Jiang, H. Jiang, K. Melcher, B. L. Roth, Y. Zhang, C. Zhang, H. E. Xu, Structural insights into the human D1 and D2 dopamine receptor signaling complexes. *Cell* **184**, 931–942.e18 (2021).
22. Y. Zhuang, B. Krumm, H. Zhang, X. E. Zhou, Y. Wang, X.-P. Huang, Y. Liu, X. Cheng, Y. Jiang, H. Jiang, C. Zhang, W. Yi, B. L. Roth, Y. Zhang, H. E. Xu, Mechanism of dopamine binding and allosteric modulation of the human D1 dopamine receptor. *Cell Res.* **31**, 593–596 (2021).
23. P. Xiao, W. Yan, L. Gou, Y. N. Zhong, L. Kong, C. Wu, X. Wen, Y. Yuan, S. Cao, C. Qu, X. Yang, C. C. Yang, A. Xia, Z. Hu, Q. Zhang, Y. H. He, D. L. Zhang, C. Zhang, G. H. Hou, H. Liu, L. Zhu, P. Fu, S. Yang, D. M. Rosenbaum, J. P. Sun, Y. du, L. Zhang, X. Yu, Z. Shao, Ligand recognition and allosteric regulation of DRD1-Gs signaling complexes. *Cell* **184**, 943–956. e18 (2021).
24. J. Yin, K. Y. M. Chen, M. J. Clark, M. Hijazi, P. Kumari, X. C. Bai, R. K. Sunahara, P. Barth, D. M. Rosenbaum, Structure of a D2 dopamine receptor-G-protein complex in a lipid membrane. *Nature* **584**, 125–129 (2020).
25. B. Sun, D. Feng, M. L. H. Chu, I. Fish, S. Lovera, Z. A. Sands, S. Kelm, A. Valade, M. Wood, T. Ceska, T. S. Kobilka, F. Lebon, B. K. Kobilka, Crystal structure of dopamine D1 receptor in complex with G protein and a non-catechol agonist. *Nat. Commun.* **12**, 3305 (2021).
26. B. T. DeVree, J. P. Mahoney, G. A. Vélez-Ruiz, S. G. F. Rasmussen, A. J. Kuszak, E. Edwald, J. J. Fung, A. Manglik, M. Masureel, Y. du, R. A. Matt, E. Pardon, J. Steyaert, B. K. Kobilka, R. K. Sunahara, Allosteric coupling from G protein to the agonist-binding pocket in GPCRs. *Nature* **535**, 182–186 (2016).
27. O. Moro, J. Lameh, P. Hogger, W. Sadee, Hydrophobic amino acid in the i2 loop plays a key role in receptor-G protein coupling. *J. Biol. Chem.* **268**, 22273–22276 (1993).
28. H. R. Kim, J. Xu, S. Maeda, N. M. Duc, D. Ahn, Y. du, K. Y. Chung, Structural mechanism underlying primary and secondary coupling between GPCRs and the Gi/o family. *Nat. Commun.* **11**, 3160 (2020).
29. P. Xu, S. Huang, C. Mao, B. E. Krumm, X. E. Zhou, Y. Tan, X. P. Huang, Y. Liu, D. D. Shen, Y. Jiang, X. Yu, H. Jiang, K. Melcher, B. L. Roth, X. Cheng, Y. Zhang, H. E. Xu, Structures of the human dopamine D3 receptor-Gi complexes. *Mol. Cell* **81**, 1147–1159.e4 (2021).
30. B. K. Kobilka, T. S. Kobilka, K. Daniel, J. W. Regan, M. G. Caron, R. J. Lefkowitz, Chimeric α2-,β2-adrenergic receptors: Delineation of domains involved in effector coupling and ligand binding specificity. *Science* **240**, 1310–1316 (1988).
31. N. M. Duc, H. R. Kim, K. Y. Chung, Structural mechanism of G protein activation by G protein-coupled receptor. *Eur. J. Pharmacol.* **763**, 214–222 (2015).
32. N. M. Duc, H. R. Kim, K. Y. Chung, Recent progress in understanding the conformational mechanism of heterotrimeric G protein activation. *Biomol. Ther. (Seoul)* **25**, 4–11 (2017).
33. B. Zhang, Y. Zhang, Z. Wang, Y. Zheng, The role of Mg^{2+} cofactor in the guanine nucleotide exchange and GTP hydrolysis reactions of Rho family GTP-binding proteins. *J. Biol. Chem.* **275**, 25299–25307 (2000).
34. M. Natochin, M. Moussaif, N. O. Artemyev, Probing the mechanism of rhodopsin-catalyzed transducin activation. *J. Neurochem.* **77**, 202–210 (2001).
35. T. Flock, C. N. J. Ravarani, D. Sun, A. J. Venkatakrishnan, M. Kayikci, C. G. Tate, D. B. Veprintsev, M. M. Babu, Universal allosteric mechanism for Gα activation by GPCRs. *Nature* **524**, 173–179 (2015).
36. D. Hilger, K. K. Kumar, H. Hu, M. F. Pedersen, E. S. O'Brien, L. Giehm, C. Jennings, G. Eskici, A. Inoue, M. Lerch, J. M. Mathiesen, G. Skiniotis, B. K. Kobilka, Structural insights into differences in G protein activation by family A and family B GPCRs. *Science* **369**, eaba3373 (2020).
37. N. Kapoor, S. T. Menon, R. Chauhan, P. Sachdev, T. P. Sakmar, Structural evidence for a sequential release mechanism for activation of heterotrimeric G proteins. *J. Mol. Biol.* **393**, 882–897 (2009).
38. R. K. Sunahara, J. J. Tesmer, A. G. Gilman, S. R. Sprang, Crystal structure of the adenylyl cyclase activator $G_{sα}$. *Science* **278**, 1943–1947 (1997).
39. B. Carpenter, C. G. Tate, Engineering a minimal G protein to facilitate crystallisation of G protein-coupled receptors in their active conformation. *Protein Eng. Des. Sel.* **29**, 583–594 (2016).
40. A. M. Preininger, N. van Eps, N. J. Yu, M. Medkova, W. L. Hubbell, H. E. Hamm, The myristoylated amino terminus of $Gα_{i1}$ plays a critical role in the structure and function of $Gα_{i1}$ subunits in solution. *Biochemistry* **42**, 7931–7941 (2003).
41. A. M. Preininger, J. Parello, S. M. Meier, G. Liao, H. E. Hamm, Receptor-mediated changes at the myristoylated amino terminus of $Gα_{il}$ proteins. *Biochemistry* **47**, 10281–10293 (2008).
42. R. Graf, R. Mattera, J. Codina, M. K. Estes, L. Birnbaumer, A truncated recombinant alpha subunit of Gi3 with a reduced affinity for beta gamma dimers and altered guanosine 5′-3-O-(thio)triphosphate binding. *J. Biol. Chem.* **267**, 24307–24314 (1992).
43. S. Zheng, N. Abreu, J. Levitz, A. C. Kruse, Structural basis for KCTD-mediated rapid desensitization of GABAB signalling. *Nature* **567**, 127–131 (2019).
44. S. Q. Zheng, E. Palovcak, J. P. Armache, K. A. Verba, Y. Cheng, D. A. Agard, MotionCor2: Anisotropic correction of beam-induced motion for improved cryo-electron microscopy. *Nat. Methods* **14**, 331–332 (2017).
45. A. Punjani, J. L. Rubinstein, D. J. Fleet, M. A. Brubaker, cryoSPARC: Algorithms for rapid unsupervised cryo-EM structure determination. *Nat. Methods* **14**, 290–296 (2017).
46. D. Asarnow, E. Palovcak, Y. Cheng, UCSF pyem v0.5. (Zenodo, 2019).
47. S. H. Scheres, RELION: Implementation of a Bayesian approach to cryo-EM structure determination. *J. Struct. Biol.* **180**, 519–530 (2012).
48. R. Sanchez-Garcia, J. Gomez-Blanco, A. Cuervo, J. M. Carazo, C. O. S. Sorzano, J. Vargas, DeepEMhancer: A deep learning solution for cryo-EM volume post-processing. *Commun. Biol.* **4**, 874 (2021).
49. A. Waterhouse, M. Bertoni, S. Bienert, G. Studer, G. Tauriello, R. Gumienny, F. T. Heer, T. A. P. de Beer, C. Rempfer, L. Bordoli, R. Lepore, T. Schwede, SWISS-MODEL: Homology modelling of protein structures and complexes. *Nucleic Acids Res.* **46**, W296–W303 (2018).
50. E. F. Pettersen, T. D. Goddard, C. C. Huang, G. S. Couch, D. M. Greenblatt, E. C. Meng, T. E. Ferrin, UCSF Chimera—A visualization system for exploratory research and analysis. *J. Comput. Chem.* **25**, 1605–1612 (2004).
51. P. Emsley, K. Cowtan, Coot: Model-building tools for molecular graphics. *Acta Crystallogr. D Biol. Crystallogr.* **60**, 2126–2132 (2004).
52. P. D. Adams, P. V. Afonine, G. Bunkóczi, V. B. Chen, I. W. Davis, N. Echols, J. J. Headd, L. W. Hung, G. J. Kapral, R. W. Grosse-Kunstleve, A. J. McCoy, N. W. Moriarty, R. Oeffner, R. J. Read, D. C. Richardson, J. S. Richardson, T. C. Terwilliger, P. H. Zwart, PHENIX: A comprehensive python-based system for macromolecular structure solution. *Acta Crystallogr. D Biol. Crystallogr.* **66**, 213–221 (2010).
53. V. B. Chen, W. B. Arendall III, J. J. Headd, D. A. Keedy, R. M. Immormino, G. J. Kapral, L. W. Murray, J. S. Richardson, D. C. Richardson, MolProbity: All-atom structure validation for macromolecular crystallography. *Acta Crystallogr. D Biol. Crystallogr.* **66**, 12–21 (2010).
54. B. A. Barad, N. Echols, R. Y. R. Wang, Y. Cheng, F. DiMaio, P. D. Adams, J. S. Fraser, EMRinger: Side chain-directed model and map validation for 3D cryo-electron microscopy. *Nat. Methods* **12**, 943–946 (2015).
55. A. Inoue, F. Raimondi, F. M. N. Kadji, G. Singh, T. Kishi, A. Uwamizu, Y. Ono, Y. Shinjo, S. Ishida, N. Arang, K. Kawakami, J. S. Gutkind, J. Aoki, R. B. Russell, Illuminating G-protein-coupling selectivity of GPCRs. *Cell* **177**, 1933–1947.e25 (2019).

Acknowledgments: We thank A. C. Kruse for the critical reading of this manuscript. We thank the staff at Shuimu BioSciences for the help with cryo-EM data collection. All EM images were collected at Shuimu BioSciences. **Funding:** This work was supported by the Chinese Ministry of Science and Technology, Beijing Municipal Science and Technology Commission (Z201100005320012), and Tsinghua University. **Author contributions:** X.T. purified and assembled the protein complex. X.T. and S.Z. collected cryo-EM data and performed cryo-EM data processing and model building. X.T. and S.C. did the cAMP accumulation assay. X.T. performed the GTP exchange assay. S.C. performed the NanoBiT assay. X.W. purified the Gβγ protein. Q.W., Z.C., and N.H. helped with structural analysis using MD. S.Z. wrote the manuscripts with input from all the other authors. **Competing interests:** The authors declare that they have no competing interests. **Data and materials availability:** The atomic structures have been deposited at the PDB under the accession codes 7F0T, 7F1O, 7F1Z, 7F23, and 7F24. The EM maps have been deposited at the Electron Microscopy Data Bank (EMDB) under the accession numbers EMD-31404, EMD-31421, EMD-31425, EMD-31426, and EMD-31427. All data needed to evaluate the conclusions in the paper are present in the paper and/or the Supplementary Materials.

Submitted 2 February 2022
Accepted 28 April 2022
Published 10 June 2022
10.1126/sciadv.abo4158